Algorithm Theoretical Basis Document for Land Surface Temperature (LST)

PRODUCTS: LSA-001 (MLST), LSA-050 (MLST-R)

Reference Number:	SAF/LAND/IM/ATBD_MLST/1.2
Issue/Revision Index:	Issue 2
Last Change:	2/06/2017

DOCUMENT SIGNATURE TABLE

	Name	Date	Signature
Prepared by :	I. Trigo, S. Freitas, J. Bioucas-Dias, C. Barroso, I. Monteiro, P. Viterbo, J.P. Martins		
Approved by:	Land SAF Project Manager (IPMA)		

DOCUMENTATION CHANGE RECORD

Issue / Revision	Date	Description:
Version 1.0	19/06/2009	Update of LST uncertainty estimations
Version 1.1	8/04/2016	Include reference to LSA-050: re-processed SEVIRI LST product. Refer LSA-002
Version 1.2	28/10/2016	Modifications suggested in ORR_EPS: - SEVIRI/MSG LST and AVHRR/Metop in separated documents. - Note on large scale uncertainty added (last paragraph of section 4.5) - Reference to snow/ice emissivity included in section 4.3.
Issue 2	02/06/2017	Added annex with description of Processing Scheme (removed from product PUM).

DISTRIBUTION LIST

Internal Consortium Distribution		
Organisation	**Name**	**No. Copies**
IPMA	Isabel Trigo	
IPMA	Isabel Monteiro	
IDL	Carlos da Camara	
IPMA	Sandra Coelho	
IPMA	Carla Barroso	
IPMA	Pedro Diegues	
IPMA	Teresa Calado	
IPMA	Pedro Ferreira	
IPMA	Ricardo Torres	
IMK	Folke-S. Olesen	
IMK	Frank Goettsche	
IMK	Ewa Kabsch	
MF	Jean-Louis Roujean	
MF	Dominique Carrer	
RMI	Françoise Meulenberghs	
RMI	Arboleda Alirio	
RMI	Nicolas Ghilain	
FMI	Niilo Siljamo	
UV	Joaquin Melia	
UV	F. Javier García Haro	
UV/EOLAB	Fernando Camacho	
UV	Aleixander Verger	

External Distribution		
Organisation	**Name**	**No. Copies**
EUMETSAT	Frédéric Gasiglia	
EUMETSAT	Cleber Balan	
EUMETSAT	Lorenzo Sarlo	
EUMETSAT	Lothar Schueller	
EDISOFT	Tiago Sepúlveda	
EDISOFT	Joana Rosa	
EDISOFT	Joaquim Araujo	
GMV	Mauro Lima	

Steering Group Distribution		
Nominated by:	**Name**	**No. Copies**
IPMA	Pedro Viterbo	
EUMETSAT	Lorenzo Sarlo	
EUMETSAT	Lothar Schueller	
EUMETSAT	Christopher Hanson	
EUMETSAT	Harald Rothfuss	
STG/AFG (USAM)	Francesco Zauli	
MF	Jean-François Mahfouf	
RMI	Rafiq Hamdi	
KIT	Johannes Orphal	
VITO	Bart Deronde	

Table of Contents

DOCUMENT SIGNATURE TABLE 2
DOCUMENTATION CHANGE RECORD 2
1. Introduction 7
2. Data Description 8
2.1. SEVIRI onboard Meteosat Second Generation 8
2.2. Calibration/Verification Database 9
2.3. Radiative Transfer Simulations 10
3. The Land-SAF LST Algorithm 11
3.1. Generalized Split-Windows 11
3.2. Calibration/Validation of the GSW Algorithm 12
4. Error Propagation 14
4.1. Framework 15
4.2. Impact of Sensor Noise 16
4.3. Impact of uncertainties in Surface Emissivity 17
4.4. Uncertainties in forecasts of atmospheric water vapour content 18
4.5. Uncertainty of LST Retrievals 21
5. Concluding Remarks 23
6. References 25
Annex - SEVIRI/Meteosat LST Product: LSA-001 (MLST)

List of Tables

Table 1 Central wavenumber and band-correction coefficients for SEVIRI thermal windows channels onboard MSG-1 and MSG-2, respectively (http://www.eumetsat.int). 11

List of Figures

Figure 1 Spectral response functions of SEVIRI thermal windows channels, centred at 10.8 and 12.0 μm, respectively, onboard MSG1, MSG2 and MSG3. 8
Figure 2 Distribution of the GSW parameters (indicated in the top of each panel) and explained variance of the fitted regression (bottom left) as a function of the satellite zenith angle and total column water vapour (mm). 13
Figure 3 Distribution of LST errors obtained for the GSW verification database, which are obtained for different classes of Satellite Zenith Angle (indicated in the bottom left of each panel) and water vapour content (W; x-axis in each diagram). The lines within each boxplot correspond to the lower quartile, median and upper quartile, respectively, while the whiskers extend to remaining data. 14
Figure 4 Histograms of LST errors (K) attributed to the sensor noise, obtained for different classes of total column water vapour; from top to bottom: 0 – to – 1.5 cm; 1.5 – to – 3.0 cm; 3.0 – to – 4.5 cm; and 4.5 – to – 6.0 cm. 16
Figure 5 As in Figure 4, but for errors in LST (K) attributed to uncertainties in surface emissivity. 18
Figure 6 Histograms of W errors (cm) – difference between forecasts and the respective analysis – for different classes of total column water vapour; from top to bottom: 0 – to – 1.5 cm; 1.5 – to – 3.0 cm; 3.0 – to – 4.5 cm; and 4.5 – to – 6.0 cm. 20
Figure 7 (a) Probability (shaded boxes) of a reference value W (horizontal axis) being forecast as W_Estimate (vertical axis), and LST errors (contours; K) associated to W forecast errors, for all possible SZA up to 77.5º; (b) contours of errors of LST retrievals obtained for all admissible classes of water vapour (W) and satellite zenith angle (SZA), taking into account the statistics of ECMWF forecast errors for W. 21
Figure 8 Histograms of LST uncertainties [K] including all sources of errors grouped by W. 22
Figure 9 (a) LST (ºC) retrievals for the 7:15 UTC time-slot of the 23rd March 2008 and (b) respective error bars (ºC); the diamonds show the relative contribution of uncertainty in emissivity ("north"), water vapour content ("east"), sensor noise ("west") and uncertainty in the GSW associated with specific retrieval conditions ("south"). 24
Figure 10. Diagram of processing chain, for SEVIRI/MSG retrieved EM (left) and LST (right). 30

1. Introduction

This document details the algorithm used for the retrieval of Land Surface Temperature (LST) from the Spinning Enhanced Visible and Infrared Imager (SEVIRI) onboard Meteosat Second Generation (MSG) satellites. The sections below describe the theoretical basis for LST estimation, together with the processing of the respective error budget. The methodology detailed here applies to near real time LST products – MLST with product identifier LSA-001 – as well as to the re-processed LST dataset – MLST-R with product identifier LSA-050. The same methodology has also been applied to LSA SAF product LSA-002, i.e., LST derived from the Advanced Very High Resolution Radiometer (AVHRR) on-board EUMETSAT polar system satellites, the Metop series.

The EUMETSAT Satellite Application Facility on Land Surface Analysis (Land-SAF) generates, on an operational basis, Land Surface Temperature (LST) from SEVIRI onboard MSG (Schmetz et al., 2002a). LST is an important parameter for the monitoring of surface energy budget, since it is the primary variable determining the upward thermal radiation and one of the main controllers of sensible and latent heat fluxes between the surface and the atmosphere. Thus, the reliable and long-term estimation of LST is extremely important for a wide number of applications, including amongst others: (i) model validation (Trigo and Viterbo, 2001; Mitchell et al. 2004), (ii) data assimilation (Caparrini et al., 2004; Qin et al, 2007; Bosilovich et al., 2007); (iii) hydrological applications (Kustas et al., 1996; Wan et al., 2004); and (iv) climate monitoring (Jin, 2004; Jin et al., 2005, Yu et al, 2008). The Land-SAF LST is processed at the full SEVIRI temporal and spatial resolution allowing the capture of the full diurnal cycle over clear sky regions.

LST estimations from remotely sensed data are generally obtained from one or more channels within the thermal infrared atmospheric window from 8-to-13 μm (Dashet al., 2002). Operational LST retrievals often make use of split-window algorithms (e.g., Prata, 1993; Wan and Dozier, 1996), where LST is obtained through a semi-empirical regression of top-of-atmosphere (TOA) brightness temperatures of two pseudo-contiguous channels, i.e., the split-window channels. The Land-SAF LST algorithm is based on the generalised split-window (GSW) formulation initially developed for AVHRR and MODIS (Wan and Dozier, 1996), adapted to SEVIRI split-window channels. The error of LST retrievals via GSW depends on (i) the uncertainty of surface emissivity, (ii) the water vapour content of the atmosphere, and (iii) or the satellite view angle. Because the latter determines the total optical path, LST estimations are often limited to satellite zenith angles (SZA) below ~60^{o}, where retrieval errors are still acceptable (e.g., Wan and Dozier, 1996 ; Sun and Pinker, 2003; Jiménez-Muñoz amd Sobrino, 2006). In the case of geostationary platforms, already unable to provide the global coverage of polar-orbiters, such view angle restrictions pose additional limitations to the product spatial coverage. A wider retrieval area must be carefully weighted against an increasing error.

Any parameter inference is of little usefulness without an uncertainty measure. Here, we discuss the calibration of the GSW algorithm used operationally by the Land-SAF and the respective assessment of LST retrieval errors. These errors take into account the expected performance of the GSW under different atmospheric conditions,

as well as the characterization of input uncertainties and their propagation to the final LST estimation.

2. Data Description

2.1. SEVIRI onboard Meteosat Second Generation

Meteosat Second Generation (MSG) is a series of 4 geostationary satellites to be operated by the European Organization for the Exploitation of Meteorological Satellites (EUMETSAT). The Spinning Enhanced Visible and Infrared Imager (SEVIRI) is the main sensor onboard MSG and it was designed to observe an earth disk with view zenith angles (SZA) ranging from 0º to 80º, with a temporal sampling of 15 minutes and a 3km sampling distance at the sub-satellite point. SEVIRI encompasses unique spectral characteristics and accuracy, with 12 channels covering the visible to the infrared (Schmetz et al., 2002a). The data are disseminated to users after being rectified to 0º longitude, which means the satellite viewing geometry varies slightly with the acquisition time (satellite zenith angles typically differ by less than 0.25º between consecutive observations).

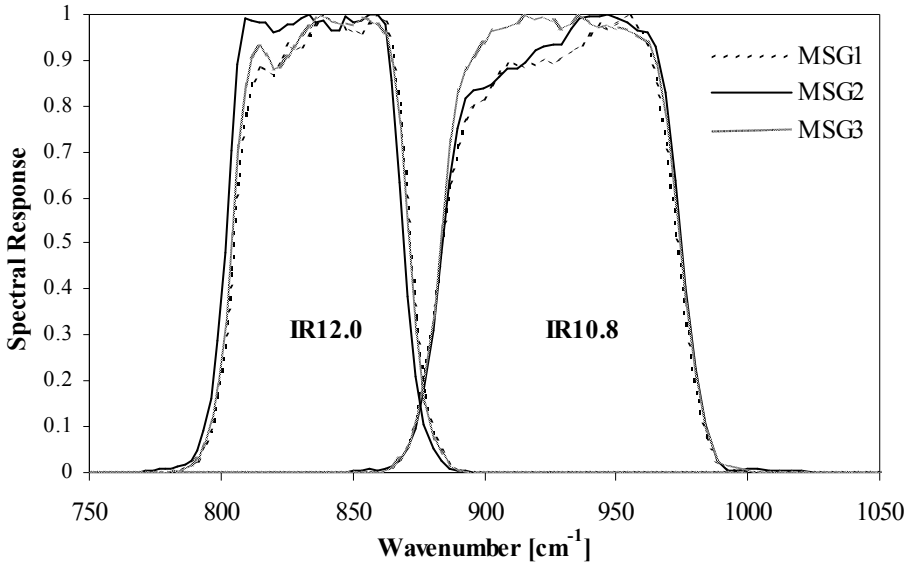

Figure 1 Spectral response functions of SEVIRI thermal windows channels, centred at 10.8 and 12.0 μm, respectively, onboard MSG1, MSG2 and MSG3.

LST is estimated from TOA brightness temperatures of SEVIRI split-window channels, centred on 10.8 and 12.0 μm (hereafter IR108 and IR120), respectively. Figure 1 shows the response functions of these two channels for MSG1, MSG2 and MSG3 (from Meteosat-8 onwards, once operational). The expected radiometric noise for IR108 (IR120) channel available onboard MSG-1 to MSG-3 is of the order of 0.11 K (0.15-0.16K; Schmetz et al. 2002b); further details may be found at EUMETSAT

website http://www.eumetsat.int. Possible inaccuracies in SEVIRI absolute or relative calibration are not considered here, despite their relevance for the quality of LST retrievals. However, it is worth mentioning that EUMETSAT has recently initiated a routine inter-calibration of SEVIRI infrared channels and the Infrared Atmospheric Sounding Interferometer (IASI; onboard EUMETSAT polar-orbiter Metop), with the aim of understanding the mechanisms for (changing) biases and developing operational corrections (Hewinson and König, 2008). Mean differences between IASI and Meteosat-8 (Meteosat-9) reported by Hewinson and König (2008) are 0.16K and 0.13K (0.03K and 0.05K), for channels IR108 and IR120, respectively.

2.2. Calibration/Verification Database

The calibration (and verification) of the GSW presented here relies on radiative transfer simulations of TOA brightness temperatures for SEVIRI channels IR108 and IR120. The simulations are performed for the database of global profiles of temperature, moisture, and ozone compiled by Borbas et al. (2005) for clear sky conditions, and referred to as SeeBor. The database contains over 15,700 profiles taken from other datasets, such as NOAA88 (Seemann et al., 2003), TIGR-like (Chevallier, 2001), and TIGR (Chedin et al., 1996), that are representative of a wide range of atmospheric (clear sky) conditions over the whole globe. In addition, surface parameters such as skin temperatures (Tskin) and a landcover classification within the International Geosphere-Biosphere Programme ecosystem categories (IGBP) (Belward, 1996) are assigned to each profile. Skin temperature over land surfaces corresponds to LST in SeeBor and is estimated as a function of 2m temperature (T2m), and solar zenith and azimuth angles (Borbas et al. 2005).

We assume that each profile corresponds to one given pixel within the Meteosat disk. Thus, for radiative simulation purposes, a SZA chosen randomly within the 0^o - 80^o range is assigned to each profile, except for cases with (i) Tskin below 270 K, which are constrained to angles above 30^o; and (ii) Tskin < 240 K, which are allowed to be observed by a geostationary satellite with a zenith angle within 60 ^{o} and 80^o. This procedure ensures a realistic cover of simulated radiances for all possible viewing geometries.

The SeeBor database described above was split into two subsets – one used for the calibration of the LST GSW, and an independent one used for verification of the fitted algorithm. The former consists of 77 atmospheres selected to cover a broad variety of water vapour content (from very dry to moist conditions), leaving more than 15,600 profiles for GSW verification. The parameters in the GSW algorithm are estimated for 8 different classes of total column water vapour (W), up to 6 cm, and for 16 classes of SZA, up to 75^o, ensuring that all ranges of atmospheric attenuation within the thermal infrared are covered.. In order to ensure that all W and SZA class have enough representative cases to provide robust parameter estimations, the radiative transfer simulations are performed over the 77 atmospheric profiles with the following settings: (i) surface temperature ranging between Tskin–15 and Tskin+15 K in steps of 5K; (ii) channel emissivities of IR108 and IR120 (ε_{108} and ε_{120}, respectively) covering

the range $0.96<\varepsilon_{120}<0.995$ in steps of 0.0175 and $\varepsilon_{120}-0.030<\varepsilon_{108}<\varepsilon_{120}+0.018$ in steps of 0.006 (excluding cases with the average of ε_{108} and ε_{120} below 0.94); and (iii) SZA ranging from nadir to 75º in steps of 5º. It is worth noting that the whole simulations cover a range of Tskin between 230 K and 341 K, and a range of [Tskin minus T2m] from -20 to +33 K. The number of different atmospheric and surface profiles obtained by exhausting all the combinations of surface temperature, channel emissivities, and SZA are 189728, yielding an equal number of radiative transfer simulations.

2.3. Radiative Transfer Simulations

The MODerate spectral resolution atmospheric TRANSsmittance algorithm (MODTRAN4) (Berk et al., 2000) provides a useful tool to quantify the radiation emitted by the surface within known atmospheric conditions that reaches a sensor operating in a specific spectral band. The radiance (L_ν) is estimated using MODTRAN4, for the bands corresponding to SEVIRI IR108 and IR120 channels, with a spectral resolution of 1 cm^{-1}. The integration of L_ν weighted by the i-th channel response function $\phi_{i,\nu}$, (see Fig. 1) provides channel i effective radiance:

$$L_i = \frac{\int_{\nu_{i,1}}^{\nu_{i,2}} \phi_{i,\nu} L_\nu d\nu}{\int_{\nu_{i,1}}^{\nu_{i,2}} \phi_{i,\nu} d\nu} \quad (1)$$

where $\nu_{i,1}$ and $\nu_{i,2}$ are the lower and upper wavenumber boundaries of the channel, respectively; the integrals in (1) are estimated taking into account the full tabulated values of the response function $\phi_{i,\nu}$, i.e., between $\nu_1 = 781.25$ cm^{-1} and $\nu_2 = 1136.36$ cm^{-1}, for channel IR108, and between $\nu_1 = 714.28$ cm^{-1} and $\nu_2 = 1000.00$ cm^{-1}, for channel IR120.

The simulated SEVIRI radiances for channel i, L_i, are then converted to equivalent black-body brightness temperatures (Tb_i) following the analytic formulation based on the Planck function (Schmetz et al, 2002c):

$$Tb_i = \left[\frac{C_2 \nu_{i,c}}{\log\left(\frac{C_1 \nu_{i,c}^3}{L_i} + 1 \right)} - \beta_i \right] \cdot \frac{1}{\alpha_i} \quad (2)$$

where $\nu_{i,c}$ is channel i central wavenumber (Table 1), $C_1=2hc^2$ and $C_2=hc/k$ (h is the Plancks constant, c the speed of light and k the Boltzmann constant). The parameters α_i and β_i, shown in Table 1 for MSG-1 and MSG-2, are band-correction coefficients, adjusted to SEVIRI ground characterization data. The simulations of IR108 and IR12.0 brightness temperatures are then performed for both MSG-1 and MSG-2, for the whole database (calibration and verification subsets) described in the previous sections.

Table 1 Central wavenumber and band-correction coefficients for SEVIRI thermal windows channels onboard MSG-1 and MSG-2, respectively (http://www.eumetsat.int).

Channel	MSG1			MSG2		
	ν_c (cm^{-1})	α	β (K)]	ν_c (cm^{-1})	α	β (K)
IR108	930.647	0.9983	0.625	931.700	0.9983	0.640
IR120	839.660	0.9988	0.397	836.445	0.9988	0.408

3. The Land-SAF LST Algorithm

3.1. Generalized Split-Windows

Several algorithms have been proposed to retrieve LST from remotely sensed thermal infrared data, e.g., Prata (1993), Dash et al. (2002), Sun and Pinker (2003), Sobrino and Romaguera (2004), Jiménez-Muñoz (2006), Coll et al., (2006), Yu et al. (2008) , Jiang amd Li (2008). The Land-SAF LST (Trigo et al., 2008b) is estimated using a Generalized Split-Window (GSW) algorithm with a formulation similar to that first proposed by Wan and Dozier (1996) for AVHRR and MODIS. Thus, LST is as a function of TOA brightness temperatures of SEVIRI IR108 and IR120 ($T_{10.8}$ and $T_{12.0}$, respectively):

$$LST = (A_1 + A_2\frac{1-\varepsilon}{\varepsilon} + A_3\frac{\Delta\varepsilon}{\varepsilon^2})\frac{T_{10.8}+T_{12.0}}{2} + (B_1 + B_2\frac{1-\varepsilon}{\varepsilon} + B_3\frac{\Delta\varepsilon}{\varepsilon^2})\frac{T_{10.8}-T_{12.0}}{2} + C + \Delta LST \qquad (3)$$

where ε is the average of the two channels surface emissivities, Δε their difference ($\varepsilon_{10.8}$ - $\varepsilon_{12.0}$), while A_j, B_j, (j = 1,2,3) and C are the GSW coefficients obtained by fitting equation (3) to the calibration data described above, and ΔLST is the model error; for each class of water vapour W and SZA Ψ, a set of coefficients A_j, B_j, C is inferred by minimizing the the l_2-norm of the model error ΔLST. The GSW algorithm is applied to clear sky pixels only. In the Land-SAF, cloud removal is performed using the software developed by the Nowcasting (NWC) SAF, which is based on multispectral threshold technique applied to visible, near-infrared, and thermal atmospheric window channels within SEVIRI, for each pixel of the image (Derrien and Gléau, 2005; NWC-SAF, 2007).

A relevant factor in the selection of the algorithm was its expected reliability for operational LST retrievals, both in terms of expected accuracy and timeliness considering the high (15-minute) generation frequency of SEVIRI LST fields. The latter favours the use of semi-empirical relationships between LST and TOA brightness temperatures, which are computationally efficient and free of the convergence problems of direct emissivity and temperature retrieval methods (e.g., Faysash and Smith, 1999) associated to the non-linearity of the inverse problem in remote sensing (e.g.,Rodgers, 2000). Recent studies have assessed the use of other window channels along with the split-windows IR108 and IR120, such as the infrared bands centred on 3.9 and 8.7 μm (IR39 and IR87; Sun and Pinker, 2007; Pinker et al., 2007). There are, however, several caveats regarding the use of those extra channels for LST operational retrievals, namely:

(i) the uncertainty of surface emissivity within IR39 and IR87 is considerably higher than that of channels IR108 and IR120, particularly over semi-arid regions, which cover a considerably area within the Meteosat disk (Trigo et al., 2008a); (ii) channel IR87 has a rather low dynamic range of 300K, which limits its use over very warm surfaces where measurements will be close to sensor saturation; (iii) solar contamination of daytime IR39 radiances would also need to be taken into account.

The error characterization of LST retrievals is an important component of the operational algorithm, and an important source of information for users. In this sense, points (i) and (ii) mentioned above constitute the major limitation to a "four-channel" methodology, one by increasing the retrieval error bars, and the other by adding the uncertainty of the radiometer behaviour close to saturation.

3.2. Calibration/Validation of the GSW Algorithm

The GSW parameters A_i, B_i, and C obtained by fitting equation (3) to the calibration dataset and the variance of LST explained by the regression are schematically shown in Figure 2. The coefficients vary fairly smoothly throughout the W and SZA classes, except for cases where very moist atmospheres are observed with high zenith angles. In such conditions the linear combination of the split-window channels cannot reproduce the non-linear path length effects. As a result, the explained variance of surface temperature by TOA brightness also reaches considerably lower values (below 90%; bottom right panel in Figure 2) and GSW errors increase substantially.

The GSW algorithm is verified against the independent subset of simulated TOA brightness temperatures (which excludes the calibration data). Figure 3 shows the GSW LST model error distribution within each class of W and SZA. Classes with root mean square error (RMSE) higher than 4K are omitted. These classes correspond to cases where the explained variance of the GSW within the training dataset is less than 93%, and where errors of 10K or more are commonly obtained within the verification database. Thus, we limit the operational production of LST to SZA below 67.5 when W is 3 cm or higher, and to SZA below 62.5 when W is 4.5 cm or higher.

The overall bias and RMSE of the GSW are 0.05K and 0.78K, respectively. As shown in Fig. 3, the retrieval errors tend to increase with both SZA and W. The RMSE is always below 2K for water vapour content and angles within the range of values admissible for Land-SAF LST estimations, with the exception of (i) W above 5.25 cm and SZA higher than 57.5^o; and (ii) W above 2.25 cm and SZA higher than 72.5^o where the GSW presents RMSE of the order of 3K.

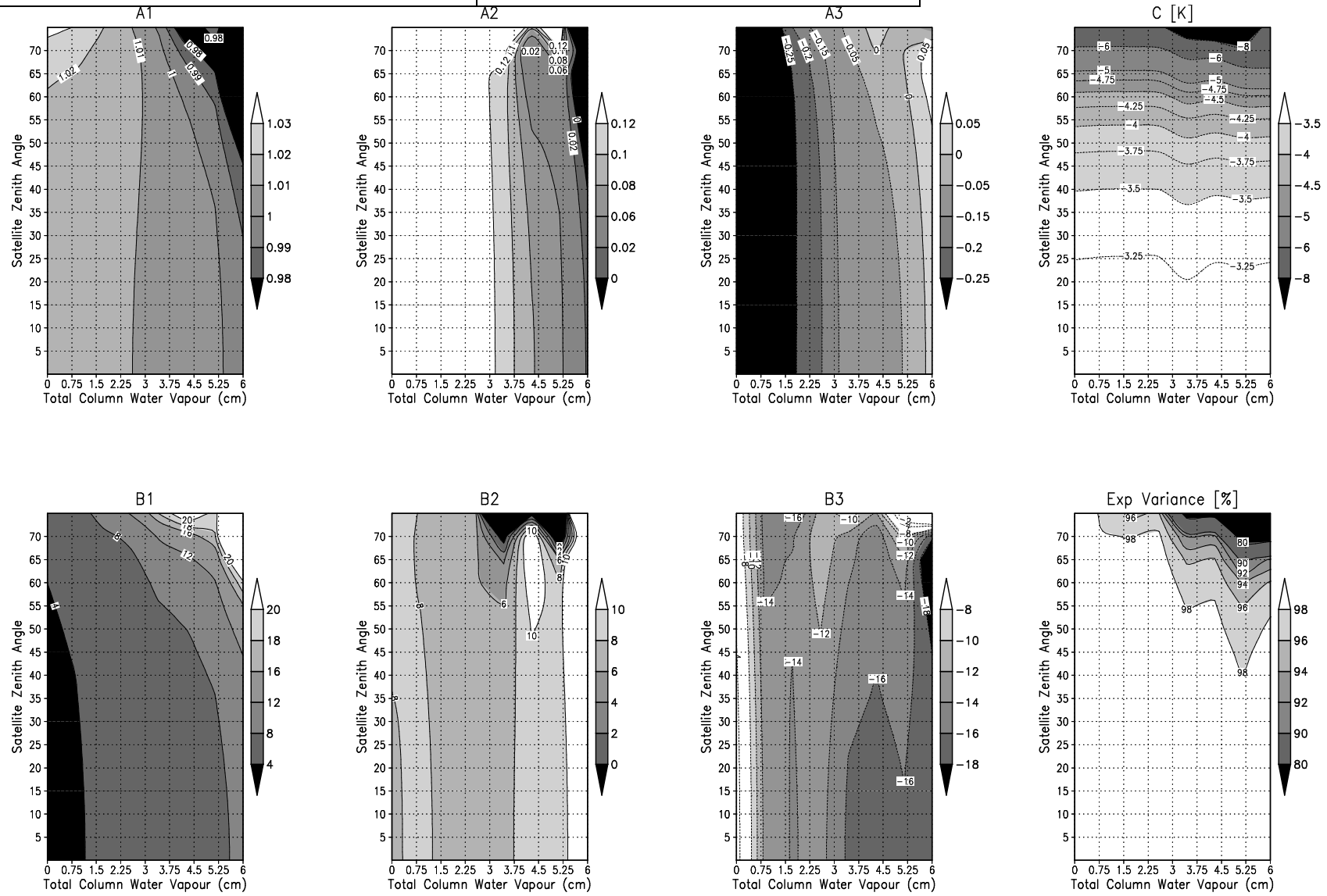

Figure 2 Distribution of the GSW parameters (indicated in the top of each panel) and explained variance of the fitted regression (bottom left) as a function of the satellite zenith angle and total column water vapour (mm).

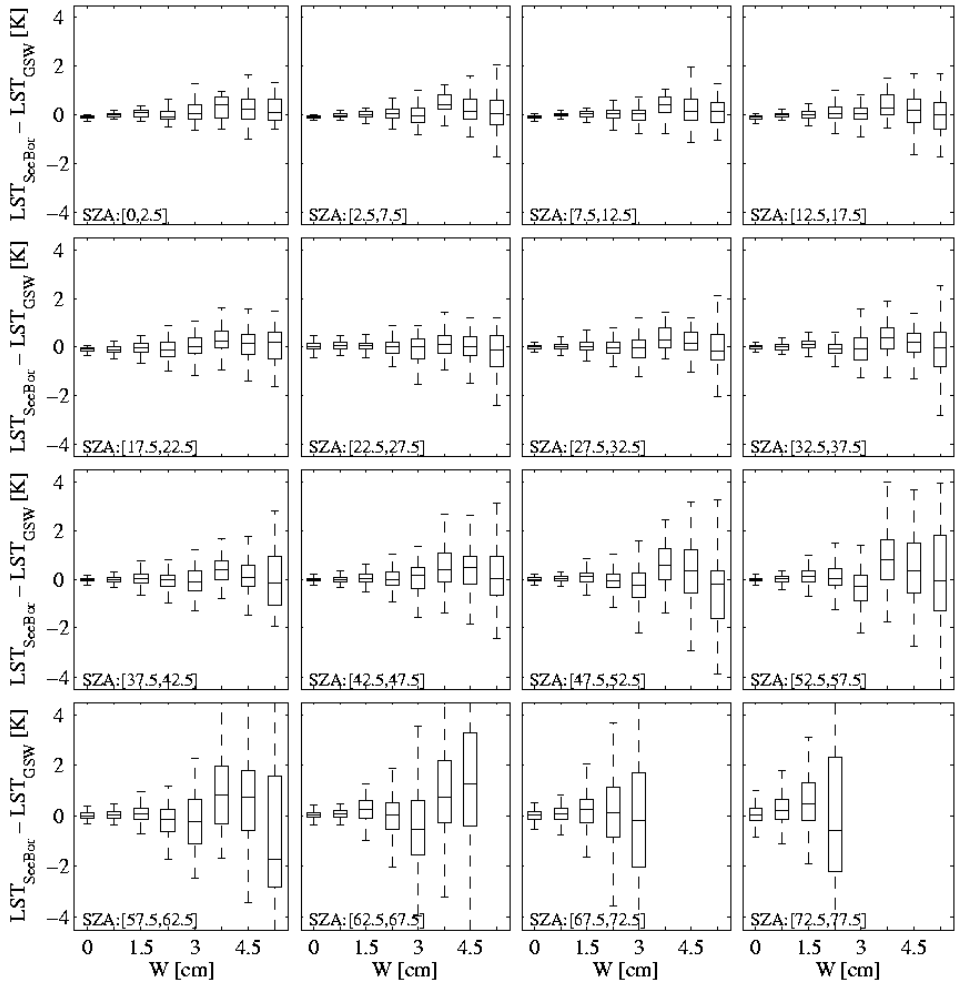

Figure 3 Distribution of LST errors obtained for the GSW verification database, which are obtained for different classes of Satellite Zenith Angle (indicated in the bottom left of each panel) and water vapour content (W; x-axis in each diagram). The lines within each boxplot correspond to the lower quartile, median and upper quartile, respectively, while the whiskers extend to remaining data.

4. Error Propagation

In a real scenario, we do not have access to the exact GSW inputs $X = (T_{10.8}, T_{12.0}, \varepsilon_{10.8}, \varepsilon_{12.0})$ and $Y = (W, \Psi)$, but only to inaccurate inputs, which we denote by $\hat{X} = (\hat{T}_{10.8}, \hat{T}_{12.0}, \hat{\varepsilon}_{10.8}, \hat{\varepsilon}_{12.0})$ and $\hat{Y} = (\hat{W}, \hat{\Psi})$. Therefore, if we still infer the LST according to model (3) replacing the exact GSW inputs with the inaccurate ones, we have a new source of error on the top of the fitting error ΔLST shown in Figure 3. In the current section, the main errors sources are identified and their impact on the total LST error estimated.

Potentially, all inputs may introduce errors in retrieved LST values. However, here we only consider the radiometric noise, the uncertainty in surface emissivity and errors in W forecasts. The rectification of the satellite data from the real position to 0º longitude may introduce errors in the determination of the SZA class. We have opted to ignore the impact of these errors on the overall LST error, taking into account that: (i) the probability of having the wrong class of SZA for MSG is fairly low, and very unlikely to be missed by more than one class; (ii) the extra GSW error induced by the wrong categorization of SZA by one class is negligible for low SZA and generally lower than 0.8K, for high SZA (above 60º).

The misclassification of cloudy pixels as clear sky would have very high impact on the retrieved LST. According to validation results of the NWC SAF cloud mask for SEVIRI, the expected rate of missed clouds is of the order of 4% (Derrien and Gléau, 2005; NWC SAF, 2007). These missed cases often correspond to broken clouds or cases in neighbouring cloudy pixels. It is very difficult to propagate the uncertainty in cloud identification to LST error bars. Instead, LST retrievals over neighbouring cloudy pixels are flagged.

4.1. Framework

Let us define the vector of model coefficients $\theta = (A_1, A_2, A_3, B_1, B_2, B_3, C)$. Notice that, the vector θ generated by the fitting process is a function of water content and view angle, i.e., $\theta = \theta(Y)$. Consider the LST estimator $\hat{LST} = f(\hat{X}, \hat{\theta})$ where $\hat{\theta} = \theta(\hat{Y})$ and $f(X, \theta)$ is the LST estimate given by model (3). A characterization of the model error is given by:

$$S_{LST} = E\left[\left(f(\hat{X}, \hat{\theta}) - LST\right)^2 \mid X, Y\right]^{1/2} \tag{4}$$

where $E[\cdot \mid X, Y]$ stands for mean value conditioned to X and Y; i.e., for a given GSW input X, Y, we want to compute the RMSE of the LST estimate. Using the fact that $LST = f(X, \theta) + \Delta LST$ and assuming that $E\left[f(\hat{X}, \hat{\theta}) \mid X, Y\right] = f(X, \theta)$, we may write:

$$S_{LST}^2 = E\left[\left(f(\hat{X}, \hat{\theta}) - f(X, \theta)\right)^2 \mid X, Y\right] + \Delta LST^2 \tag{5}$$

By taking a linear approximation of $f(\hat{X}, \hat{\theta})$ in the neighbourhood of (X, θ), and denoting $\sigma_{X_i}^2 = E\left[\left(\hat{X}_i - X_i\right)^2 \mid X\right]$ and $\sigma_{\theta_i}^2 = E\left[\left(\hat{\theta}_i - \theta_i\right)^2 \mid Y\right]$, we are led to

$$S_{LST}^2 = \sum_i \left(\frac{\partial f}{\partial X_i}\right)^2 \sigma_{X_i}^2 + \sum_j \left(\frac{\partial f}{\partial \theta_j}\right)^2 \sigma_{\theta_j}^2 + \Delta LST^2, \tag{6}$$

where we have assumed that the components of X, Y are mutually independent and that $E\left[\left(\hat{X}_i - X_i\right)|\, X\right]=0$ and $E\left[\left(\hat{\theta}_i - \theta_i\right)|\, Y\right]=0$. Next, we study in detail the error due to each individual GSW input.

4.2. Impact of Sensor Noise

The expected radiometric noise of SEVIRI channels IR108 and IR120 onboard MSG-2 is $\sigma_{T_{108}}=0.11\text{K}$ and $\sigma_{T_{120}}=0.16\text{ K}$, respectively. The associated LST uncertainty is then

$$S_{Tb}^2 = S_{Tb108}^2 + S_{Tb120}^2 \tag{7}$$

where

$$S_{Tb108}^2 = \left(\frac{\partial f}{\partial T_{108}}\right)^2 \sigma_{T_{108}}^2 \text{ and } S_{Tb120}^2 = \left(\frac{\partial f}{\partial T_{120}}\right)^2 \sigma_{T_{120}}^2 \tag{8}$$

Figure 4 shows the distributions of errors attributed to the impact of sensor noise, S_{Tb}, grouping all possible SZA within different ranges of W. S_{Tb}. is generally bellow 0.75K, and increases with the atmospheric water content. The larger variability within the moister atmospheres (bottom panel in Fig.4) is largely associated to non-linear effects on the atmospheric path for high SZA. In the most extreme cases, with W higher than 3 cm, S_{Tb} is higher than 0.5 K and may reach values above 2K.

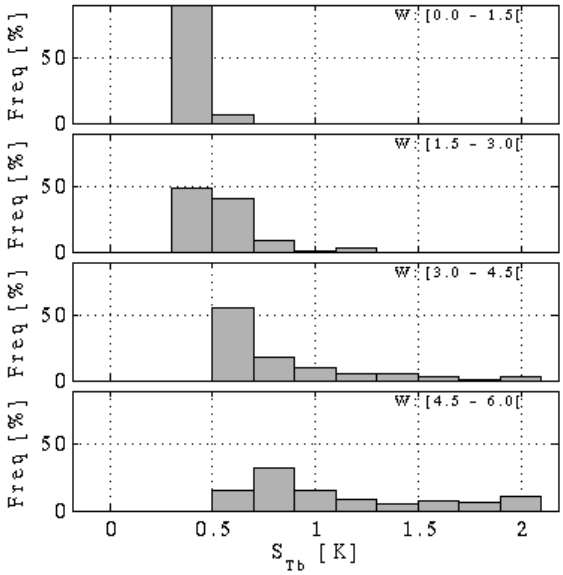

Figure 4 Histograms of LST errors (K) attributed to the sensor noise, obtained for different classes of total column water vapour; from top to bottom: 0 – to – 1.5 cm; 1.5 – to – 3.0 cm; 3.0 – to – 4.5 cm; and 4.5 – to – 6.0 cm.

4.3. Impact of uncertainties in Surface Emissivity

The impact of uncertainties in surface emissivity for channels IR108 and IR120, $\sigma_{\varepsilon_{108}}$ and $\sigma_{\varepsilon_{120}}$, respectively, on LST is given by:

$$S_{\varepsilon}^2 = S_{\varepsilon_{108}}^2 + S_{\varepsilon_{120}}^2 \tag{9}$$

where

$$S_{\varepsilon_{108}}^2 = \left(\frac{\partial f}{\partial \varepsilon_{108}}\right)^2 \sigma_{\varepsilon_{108}}^2 \quad \text{and} \quad S_{\varepsilon_{120}}^2 = \left(\frac{\partial f}{\partial \varepsilon_{120}}\right)^2 \sigma_{\varepsilon_{120}}^2 . \tag{10}$$

Emissivity retrievals are based on the so-called Vegetation Cover Method (Caselles and Sobrino, 1989; Peres and DaCamara, 2005), where effective channel emissivity for any given pixel is estimated as a weighted average of channel emissivities of dominant bareground and vegetation types within the scene. Furthermore, it is considered that SEVIRI pixels may include a land, F_{Land}, and and an in-land water fraction $(1 - F_{Land})$, and thus the effective pixel emissivity, ε_{eff_IRn}, is given by:

$$\varepsilon_{LAND\_IRn} = \varepsilon_{veg\_IRn}\, FVC + \varepsilon_{bg\_IRn}\,(1 - FVC) \tag{11a}$$
$$\varepsilon_{eff\_IRn} = \varepsilon_{LAND\_IRn}\, F_{Land} + \varepsilon_{WATER\_IRn}\,(1 - F_{Land}) \tag{11b}$$

where FVC is the pixel fraction of vegetation cover and ε_{veg_IRn}, ε_{bg_IRn}, ε_{WATER_IRn} are the vegetation, bareground, and water emissivities, respectively, for the split-window channel IRn. The values for ε_{veg_IRn} and ε_{bg_IRn} are available from look-up-tables (Table 2), determined for the land cover classes within the IGBP (Belward, 1996) database (Peres and DaCamara, 2005); in the case of inland water, ε_{WATER_IRn} is set to the Water Bodies values detailed in Table 2. Pixels identified as snow/ice (either by the cloud mask algorithm or by the H-SAF snow products) are also set to the respective emissivity tabulated values. Channel emissivity is currently estimated from FVC retrieved by the Land-SAF from SEVIRI/Meteosat (Garcia-Haro et al., 2005), and corresponds to 5-day composites updated on a daily basis.

The uncertainties in retrieved emissivity are thoroughly discussed in (Trigo et al, 2008a). These take into account inaccuracies in the VCM inputs (of the order of 0.1 for FVC; IGBP-class dependent in the case of ε_{veg_IRn} and ε_{bg_IRn}), and errors in the approximation made by equation (11), which ignores the effect of multiple reflections within the canopies/ground. A further source of emissivity errors relies on the classification of each SEVIRI pixel into one of the two categories: “land” with FLand = 1; or “water” with FLand = 0. To take this into account in the estimation of emissivity uncertainty, we assume an average error of 0.20 in FLand; in coastal pixels, this uncertainty may reach 0.45.

Error bars of channel emissivity, $\Delta\varepsilon 108$ and $\Delta\varepsilon 120$, are estimated operationally along with the emissivity values themselves, and later used for LST error bars. Here, we assess the impact of emissivity uncertainties on LST, prescribing a fixed FVC characteristic of each IGBP land cover (Table 2), and thus assigning to every profile in

the SeeBor verification database a value of ε108, ε120, Δε108 and Δε120 (Table2). On top of this, we assume FLand equal to 0 or 1, but prescribing an uncertainty of 0.2, i.e., for "land" pixels FLand may range from 0.8-to-1, while for "water pixels" FLand lies between 0 and 0.20. Figure 5 shows the results obtained for different ranges of total column water vapour. As expected, the sensitivity to land surface emissivity is significantly higher for drier atmospheres, since under moist conditions the impact of emissivity on the surface emitted radiance is partially compensated by an opposite effect on the (higher) atmospheric radiation reflected by the surface (Trigo et al., 2008a). Moreover, the higher values of Δε108 and Δε120 are often found in (semi-)arid regions (see Barren Sparsely Vegetated, Savanna, or Woody Savanna land cover types in Table 2), leading to LST inaccuracies of 1 K or more under dry conditions (W below 1.5 cm). In contrast the impact on LST is always below 2K for the moister atmospheres (W > 4.5 cm).

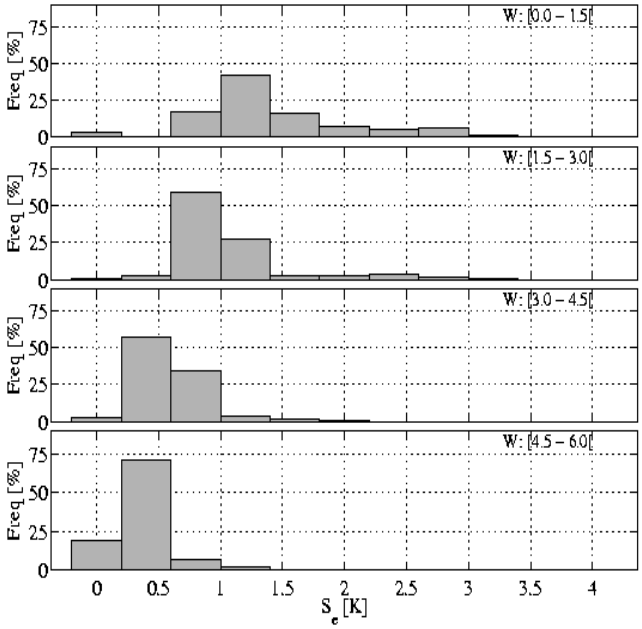

Figure 5 As in Figure 4, but for errors in LST (K) attributed to uncertainties in surface emissivity.

4.4. Uncertainties in forecasts of atmospheric water vapour content

According to the equation (6), the error due to uncertainties in the water vapour content is given by:

$$S_W^2 = \sum_j \left(\frac{\partial f}{\partial \theta_j} \right)^2 \sigma_{\theta_j}^2 \tag{12}$$

where

$$\sigma_{\theta_j}^2 = E\left[\left(\hat{\theta}_j - \theta_j \right)^2 | W, \Psi \right] \tag{13}$$

Since we neglect the uncertainty in the SZA Ψ, let us focus out attention on *W*. Given that $\hat{\theta}$ is a piece-wise linear function, we have

$$\sigma_{\theta_j}^2 = E\left[\left(\hat{\theta}_j - \theta_j\right)^2 | W\right] = \sum_k \left(\hat{\theta}_j(R_k) - \theta_j\right)^2 P(\hat{W} \in R_k | W) \quad (14)$$

where R_k is the region of the water vapour domain where the k-th linear model is assumed. Therefore the sets R_k are a partition of the referred to domain.

The operational use of the GSW algorithm (3) to retrieve LST from SEVIRI makes use of forecasts of total column water vapour (W) provided by the European Centre for Medium-range Weather Forecasts (ECMWF), for parameter selection. To characterize W error statistics, we compared ECMWF W forecasts (with forecast steps ranging between 12 and 36 h) with the respective analysis, for the 15th of each month during 2007; ECMWF grid points with model cloud cover higher than 10% were excluded. The histograms of the difference between forecasts and analyses are shown in Figure 6, for different classes of TCWV. Forecast errors could also be assessed through a comparison with observations, e.g. radiosondes, however, here we consider the model analysis to correspond to the best estimate of the state of the atmosphere at any given time. The recent evolution of assimilation techniques and assimilated data – including both conventional data such as radiosondes, and remote sensing – contributed to a significant improvement of ECMWF model analysis of water vapour content (Andersson et al., 2005). As a consequence, the bias of ECMWF humidity analysis has decreased significantly, supporting the use of analysis fields as reference for the estimation of forecast errors. Moreover, the procedure described here can also be easily reproduced whenever changes to ECMWF model justify a re-assessment of W forecasts.

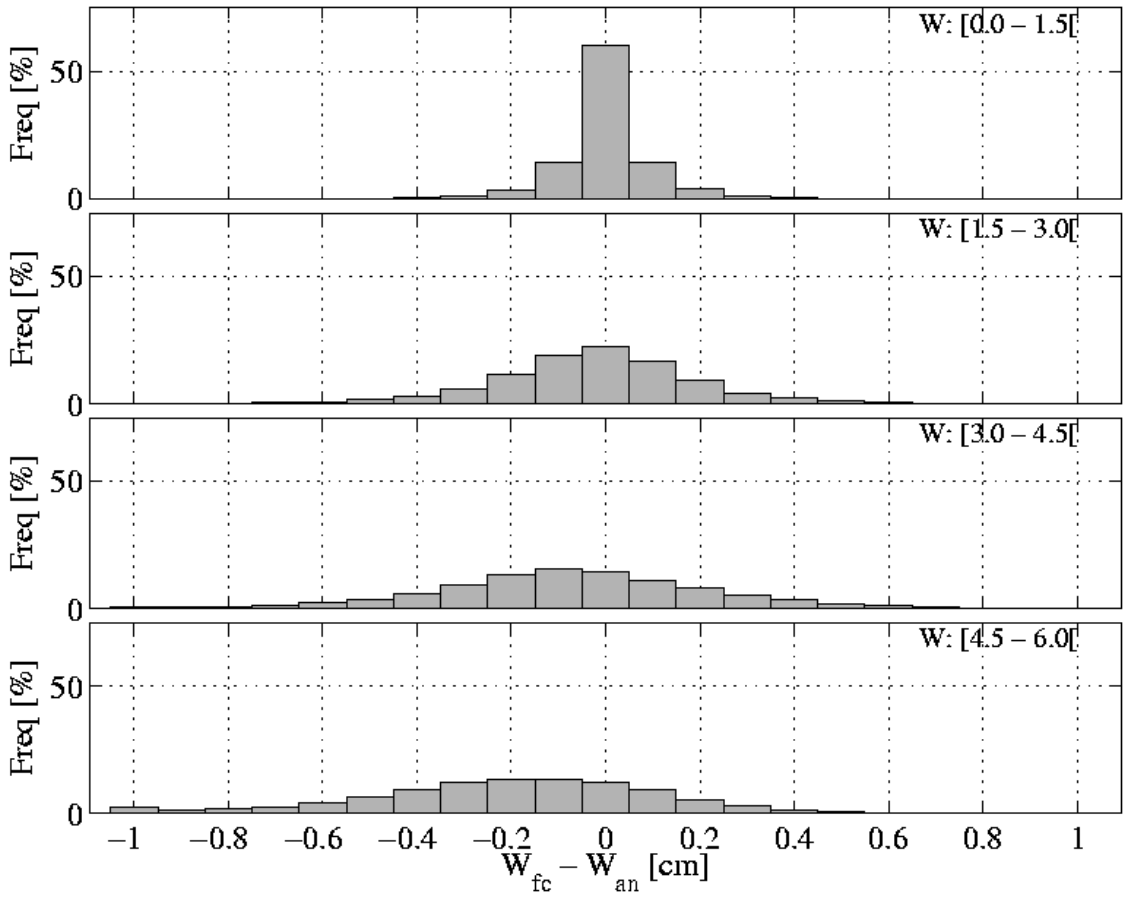

Figure 6 Histograms of W errors (cm) – difference between forecasts and the respective analysis – for different classes of total column water vapour; from top to bottom: 0 – to – 1.5 cm; 1.5 – to – 3.0 cm; 3.0 – to – 4.5 cm; and 4.5 – to – 6.0 cm.

The comparison between W forecasts and analysis (the reference value) allowed us to estimate the probability $P\left(\hat{W}_i \mid W_j\right)$, i.e., the probability that $\hat{W}$ belongs to the water vapour content class W_i, given that the true class is W_j. This probability is then used to compute the expected LST error, according to the expressions (12) to (14). Figure 7a shows shaded values of $P\left(\hat{W} \mid W\right)$ superimposed on contours of LST errors associated to $\hat{W}$ forecast errors, i.e., to the wrong choice of GSW parameters. The estimated errors of LST retrievals associated to total column water vapour uncertainties, which are obtained through the application of equations (12)-(14) to all possible classes of W and SZA, are depicted in Figure 7b. These are generally below 0.2 K for dry-to-moderately moist atmospheres. Higher values occur only for W above 5.25 cm.

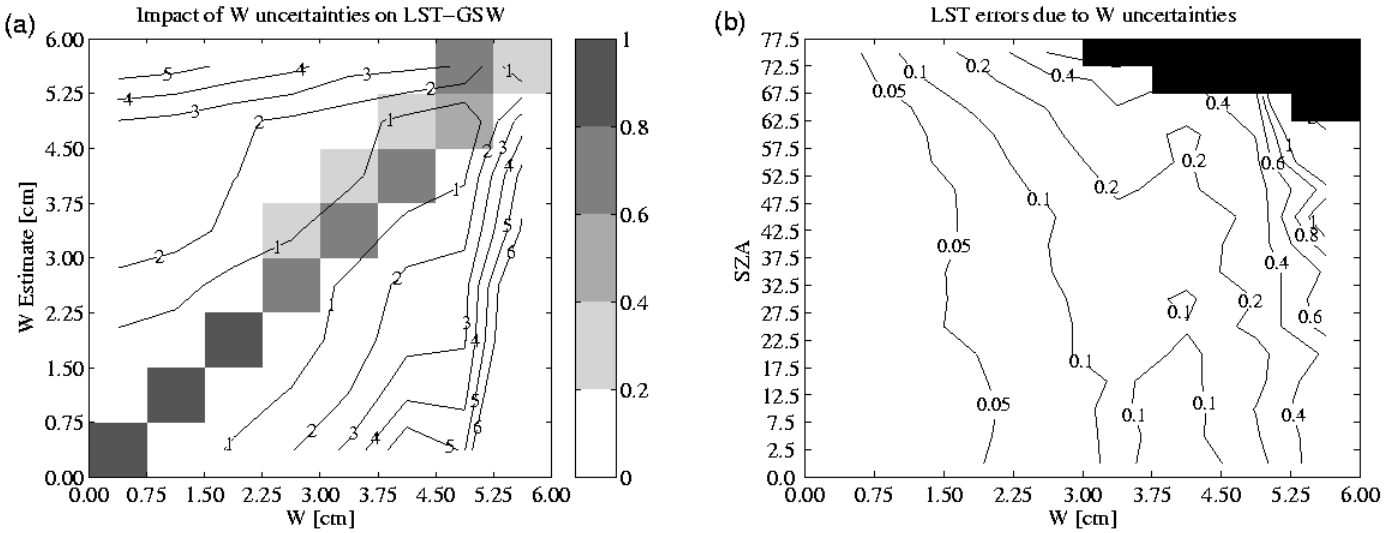

Figure 7 (a) Probability (shaded boxes) of a reference value W (horizontal axis) being forecast as W_Estimate (vertical axis), and LST errors (contours; K) associated to W forecast errors, for all possible SZA up to 77.5º; (b) contours of errors of LST retrievals obtained for all admissible classes of water vapour (W) and satellite zenith angle (SZA), taking into account the statistics of ECMWF forecast errors for W.

4.5. Uncertainty of LST Retrievals

The estimation of LST error bars, S_{LST}, assumes that all sources of errors described in the previous sections are independent:

$$S_{LST} = \sqrt{S_{Tb}^2 + S_{\varepsilon}^2 + S_W^2 + \Delta LST^2} \tag{15}$$

Figure 8 shows histograms of LST uncertainties for four non-overlapping ranges of W. These were obtained for "LST retrievals" computed for the validation dataset described in section II.B and taking into account the uncertainties of the different input variables, as discussed above. Dry atmospheres present the widest range of S_{LST}. In such conditions, the total error depends essentially on emissivity uncertainties and to a lesser extent on the view zenith angle. Nevertheless, S_{LST} distributions tend to be shifted to the right with total water vapour content, i.e., LST error bars increase for higher optical depths.

The MLST product will be affected by large-scale systematic uncertainties. However, it should be stressed that the most likely source of systematic uncertainties in the LSA SAF LST products arises from systematic errors in surface emissivity. Given its low variability in time, errors in the bareground or vegetation emissivity attributed to any given pixel translates into a source of systematic errors, particularly relevant in arid and sparsely vegetated regions.

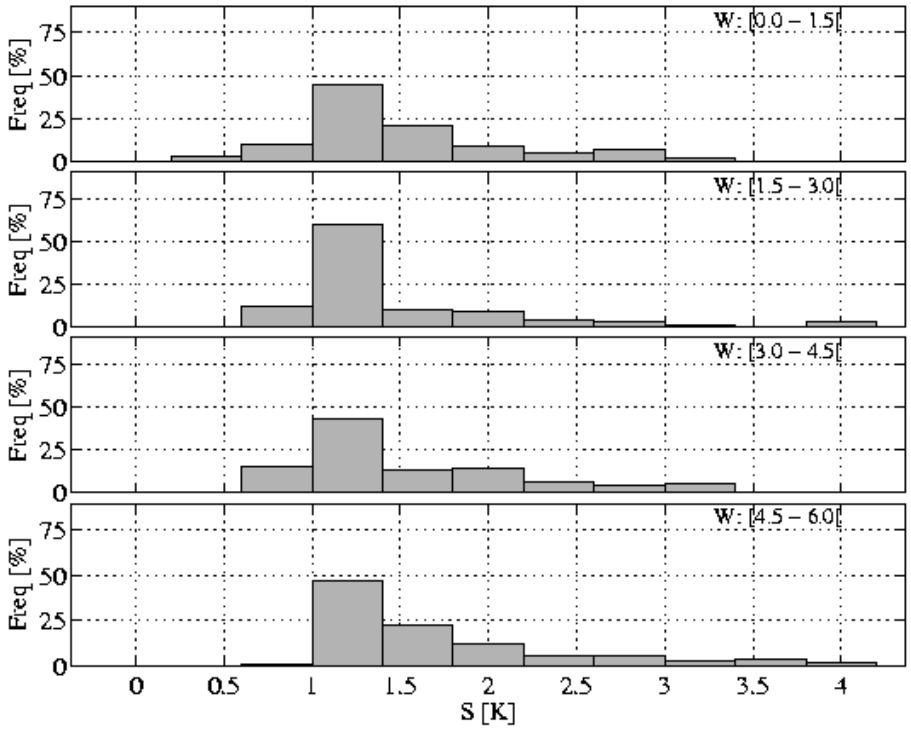

Figure 8 Histograms of LST uncertainties [K] including all sources of errors grouped by W.

5. Concluding Remarks

The Generalised Split-Window (GSW) algorithm is a semi-empirical algorithm that allows the estimation of LST from top-of-atmosphere brightness temperatures of two adjacent channels within the atmospheric window part of the spectrum, assuming the channel surface emissivities are known. A version of the GSW was trained for the series of Meteosat Second Generation (MSG) satellites and is currently used for operational retrievals of LST by the Land-SAF. To maximize the algorithm performance over a wide range of conditions, the GSW parameters are tuned for classes of satellite view angle and total column water vapour (Wan and Dozier, 1996).

A reliable estimation of the uncertainty of remote sensing retrievals is often essential for the optimal use of the retrieved parameter. This work focuses on the quantification of error bars associated to LST estimations from SEVIRI/MSG through a careful characterization of: (i) the uncertainty of the GSW algorithm itself, which is highly dependent on the retrieval conditions – view angle and atmospheric water vapour content; (ii) the uncertainty of the input variables and their propagation through the GSW algorithm. For the latter, we take into account the expected sensor noise for the SEVIRI window channels onboard the MSG series, the error bars of surface emissivity retrievals (discussed in Trigo et al., 2008a) and forecast errors of total column water vapour (W). Since the GSW is applicable to clear sky pixels only, the misclassification of a (partially) cloud-covered scene would lead to erroneous LST values. The resulting error is difficult to estimate a priori, as it depends on, e.g., the extent of the cloud cover, or cloud top height. Considering that the overall performance of the cloud mask used is fairly good (Derrien and Gléau, 2005), the LST error bars do not take into account the uncertainty of the pixel classification, but instead the cloud mask confidence is made available to the user through the LST quality flag.

Satellite zenith view angle (SZA) and W are implicit input variables for LST retrievals, in the sense that their values are used to determine the best set of GSW parameters (A_i, B_i, and C in equation (3)). The uncertainty of ~1/3 pixel in the geolocation of level 1.5 SEVIRI data has a marginal effect on LST error bars, since only pixels with SZA close to the upper/lower limits may risk being misclassified to a neighbouring SZA class. The probability of choosing inappropriate GSW parameters due to a misclassification of W is estimated from error statistics of humidity forecasts of the current version of ECMWF model; the procedure described in the current work can easily be duplicated for future model releases. Such probability is then combined with the results of a sensitivity analysis of the GSW to estimate their contribution to LST error bars.

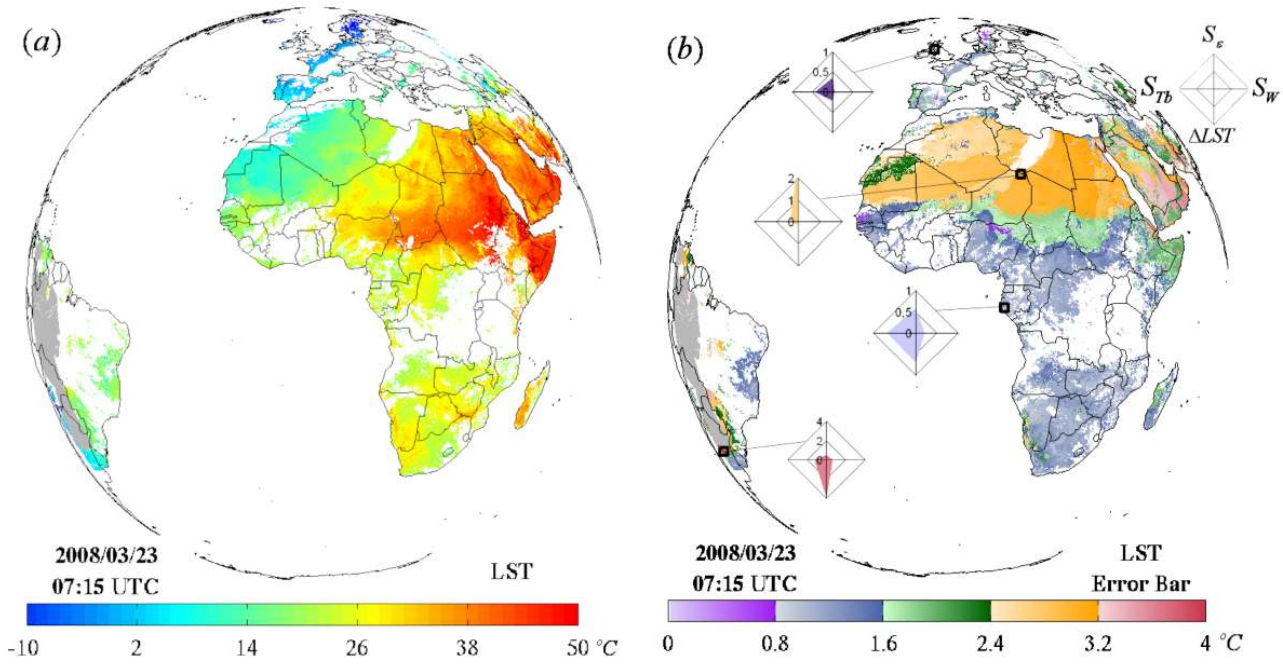

Figure 9 (a) LST (ºC) retrievals for the 7:15 UTC time-slot of the 23rd March 2008 and (b) respective error bars (ºC); the diamonds show the relative contribution of uncertainty in emissivity ("north"), water vapour content ("east"), sensor noise ("west") and uncertainty in the GSW associated with specific retrieval conditions ("south").

The spatial coverage of LST retrievals from SEVIRI/MSG data presented here is then essentially based on the respective uncertainty, in contrast with most (split-window) algorithms for LST, where estimations are restricted to SZA below a fixed threshold (often ~60º; e.g., Wan and Dozer, 1996; Sun and Pinker, 2003). Within the MSG disk the atmosphere is often fairly dry for clear sky conditions and for relatively large (~60º – 70º) SZA, partially compensating for the poorer performance of the GSW algorithm due to the long optical path. Figure 9 presents one such example, where parts of Northern Europe, the Middle East and Saudi Arabia, which are cloud free, present a relatively low atmospheric water vapour content, which allow the estimation of LST with a reasonable degree of accuracy. The far west region of Southern America is also viewed at relatively high angles as the above-mentioned areas, but presents a much higher atmospheric humidity, which would lead to meaningless retrievals of LST. Thus, the analysis of the various error sources of remotely sensed LST allows the maximization of the product spatial coverage. In the case of LST estimation provided by the Land-SAF, LST fields are distributed along with realistic estimations of the respective error bars on a pixel-by-pixel basis, allowing users to make the ultimate decision on the applicability of the retrieved product.

6. References

Andersson, E.. P. Bauer, A. Beljaars, F. Chevallier, E. Hólm, M. Janisková, P. Kållberg, G. Kelly, P. Lopez, A. McNally, E. Moreau, A. J. Simmons, J.-N. Thépaut, and A. M. Tompkins, "Assimilation and modeling of the atmospheric hydrological cycle in the ECMWF forecasting system", *Bull. Amer. Meteorol. Soc*., vol. 86, pp. 387–402. DOI:10.1175/BAMS-86-3-387, 2005.

Belward, A. S., "The IGBP-DIS global 1km land cover data set (DISCover) – proposal and implementation plans". IGBP-DIS working paper No. 13. IGBP-DIS Office, Météo-France, Toulouse, France, 61 pp, 1996.

Berk, A., G.P. Anderson, P.K. Acharya, J.H. Chetwynd, L.S. Bernstein, E.P. Shettle, M.W. Matthew, and S.M. Alder-Golden. "MODTRAN4 Version 2 User's Manual Air Force Res. Lab.", Space Vehicles Directorate, Air Force Material Command, Hanscom AFB, MA, 2000.

Borbas, E., S. W. Seemann, H.-L. Huang, J. Li, and W. P. Menzel, "Global profile training database for satellite regression retrievals with estimates of skin temperature and emissivity". *Proc. of the Int. ATOVS Study Conference-XIV*, Beijing, China, 25-31 May 2005, pp763-770, 2005.

Bosilovich, M. G., J. D. Radakovich, A. da Silva, R. Todling, and F. Verter, "Skin temperature analysis and bias correction in a coupled land-atmosphere data assimilation system", *J. Meteorol. Soc. Japan*, vol. 85A, 205-228, 2007.

Caparrini, F., F. Castelli, and D. Entekhabi, "Variational estimation of soil and vegetation turbulent transfer and heat flux parameters from sequences of multisensor imagery" *Water Resour. Res*., vol. 40, doi:10.1029/2004WR003358, 2004.

Caselles, V. and J. A. Sobrino, "Determination of frosts in orange groves from NOAA-9 AVHRR data", *Remote Sens. Environ*., vol 29, 135–146, 1989.

Chevallier, F., "Sampled databases of 60-level atmospheric profiles from the ECMWF analyses", Numerical Weather Prediction Satellite Application Facility Research Report [NWP SAF Res. Rep.] no. 4, Jan 2002, 2001.

Chedin, A. N. A. Scott, C. Wahiche, and P. Moulinier, 1985, "The improved initialization inversion method: a high resolution physical method for temperature retrievals from satellites of the TIROS-N series", *J. Climate Appl. Meteor*., vol. 24, 128-143, 1985.

Coll, C., V. Caselles, J. M. Galve, E. Valor, R. Niclós, and J. M. Sánchez, "Evaluation of split-window and dual-angle correction methods for land surface temperature retrieval from Envisat/Advanced Along, Track Scanning Radiometer (AATSR) data", *J. Geophys. Res.,* vol. 111, D12105, doi:10.1029/2005JD006830, 2006.

Dash, P., F. M. Göttsche, F. S. Olesen and H. Fischer, "Land surface temperature and emissivity estimation from passive sensor data: theory and practice–current trends", *Int. J. Remote Sens*., vol. 23, 2563–2594, 2002.

Derrien, M. and Gléau, H. Le 2005: MSG/SEVIRI cloud mask and type from SAFNWC, *Int. J. Remote Sens*., **26**, 4707 – 4732. doi:10.1080/01431160500166128

Faysash A. and E. A. Smith, "Simultaneous land surface temperature-emissivity retrieval in the infrared split window". *J. Atmos. Oceanic Technol*., vol. 16, 1673-1689, 1999.

Garcia-Haro, F.J., S. Sommer, T. Kemper, "Variable multiple endmember spectral mixture analysis (VMESMA)", *Int. J. Remote Sens*., vol. 26, pp. 2135-2162, 2005.

Göttsche, F.-M., and F.S. Olesen, "Modelling of diurnal cycles of brightness temperatures extracted from METEOSAT data", *Remote Sens. Environ*, vol. 76, 337-348, 2001.

Göttsche, F.-M., and F.S. Olesen, "Modelling the effect of optical thickness on diurnal cycles of land surface temperature", *Remote Sens. Environ*, vol. 113, 2306-2316, 2009.

Hewison T. J., and M. König, "Inter-calibration of Meteosat imagers and IASI", *2008 EUMETSAT Meteorological Satellite Conference*, Darmstadt, Germany, 8-12 September 2008 (available at http://www.eumetsat.int), 2008.

Holben, B. N., "Characteristics of maximum-value composite images from temporal AVHRR data", *Int. J. Remote Sens.*, vol. 7, 1417–1734, 1986.

Jiang, G.-M. and Z.-L. Li, "Split-window algorithm for land surface temperature estimation from MSG1-SEVIRI data", *Int. J. Remote Sens*., vol 29, 6067–6074, 2008.

Jiménez-Muñoz, J. C. and J. A. Sobrino, "Error sources on the land surface temperature retrieved from thermal infrared single channel remote sensing data", *Int. J. Remote Sens*., vol 25, 999–1014, 2006.

Jin, M., "Analysis of land skin temperature using AVHRR observations", *Bull. Amer. Meteorol. Soc*., **85**, pp. 587–600, 2004.

Jin, M., R.E. Dickinson, and D. Zhang, "The Footprint of Urban Areas on Global Climate as Characterized by MODIS" *J. Climate*, vol. 18, 1551–1565, 2005.

Kustas, W. P., and J. M. Norman, "Use of remote sensing for evapotranspiration monitoring over land surfaces", *Hydrol. Sci. J*., vol. 41, pp. 495–515, 1996.

Lambin, E.F., and D. Ehrlich, "The surface temperature-vegetation index space for land cover and land-cover change analysis", *Int. J. Remote Sens*., vol 17, 463-487, 1996.

Martins, J. P. A., I. F. Trigo, V. A. Bento, and C. da Camara , "A Physically Constrained Calibration Database for Land Surface Temperature Using Infrared Retrieval Algorithms", *Remote Sensing*, **8**, 808; doi:10.3390/rs8100808, 2016

Mitchell, K. E. , D. Lohmann, P. R. Houser, E. F. Wood, J. C. Schaake, A. Robock, B. A. Cosgrove, J. Sheffield, Q. Duan, L. Luo, R. W. Higgins, R. T. Pinker, J. D. Tarpley, D. P. Lettenmaier, C. H. Marshall, J. K. Entin, M. Pan, W. Shi, V. Koren, J. Meng, B. H. Ramsay, and A. A. Bailey, "The multi-institution North American Land Data Assimilation System (NLDAS): Utilizing multiple GCIP products and partners in a continental distributed hydrological modeling system", *J. Geophys. Res*., vol. 109, doi: 10.1029/2003JD003823, 2004

NWC-SAF, "Algorithm Theoretical Basis Document for 'Cloud Products' " (CMa-PGE01, CT-PGE02 & CTTH-PGE03 v1.4). SAF/NWC/CDOP/MFL/SCI/ATBD/01, Issue 1, Rev. 4, 7 November 2007. (available at http://nwcsaf.inm.es/), 2007.

Park, S., Feddema, J. J., and S. L. Egbert, "MODIS land surface temperature composite data and their relationships with climatic water budget factors in the central Great Plains, *Int. J. Remote Sens*., vol 26, 1127-1144, 2005.

Peres, L. F. and C. C. DaCamara, "Emissivity Maps to Retrieve Land-Surface Temperature From MSG/SEVIRI", *IEEE Trans. Geosci. Remote Sens*., vol. 43, pp. 1834-1844, 2005.

Pinker, R. T., D. Sun, M. Miller, and G. J. Robinson, "Diurnal cycle of land surface temperature in a desert encroachment zone as observed from satellites", *Geophys. Res. Lett*., vol. 34, doi:10.1029/2007GL03186, 2007.

Prata, A. J. "Land surface temperature derived from the advanced very high resolution radiometer and the along-track scanning radiometer: 1. Theory", *J. Geophys. Res*., vol. 98, 16,689– 16,702, 1993.

Qin, J. ,S. Liang, R. Liu, H. Zhang, and B. Hu, "A Weak-Constraint-Based Data Assimilation Scheme for Estimating Surface Turbulent Fluxes", *IEEE Trans. Geosci. Remote Sens. Lett*., vol. 4, doi: 10.1109/LGRS.2007.904004, 2007.

Rodgers, C. D., "Inverse methods for atmospheric sounding: theory and practice", Series on Atmospheric, Ocean and Planetary Physics, vol. 2. World Scientific, Hackensack, 238 pp., 2000.

Schmetz, J. ,P. Pili, S. Tjemkes, D. Just, J. Kerkman, S. Rota, and A. Ratier, "An introduction to Meteosat Second Generation (MSG)", *Bull. Amer. Meteor. Soc*., vol. 83, 977-992, 2002a

Schmetz., J., P. Pili, S. Tjemkes, D. Just, J. Kerkman, S. Rota, and A. Ratier, "Radiometric performance of SEVIRI", *Bull. Amer. Meteor. Soc*., vol. 83, ES50-ES51, 2002b

Schmetz, J., P. Pili, S. Tjemkes, D. Just, J. Kerkman, S. Rota, and A. Ratier, "SEVIRI calibration", *Bull. Amer. Meteor. Soc*., vol 83, ES52-ES53, 2002c.

Seemann, S. W., J. Li, W. P. Menzel, and L. E. Gumley, "Operational retrieval of atmospheric temperature, moisture, and ozone from MODIS infrared radiances". *J. Appl. Meteor*., vol 42, 1072-1091, 2003

Sobrino, J.A., M. Romaguera, "Land surface temperature retrieval from MSG1-SEVIRI data", *Remote Sens. Environ*., vol 92, 247–254, 2004.

Sun, D. and R. T. Pinker, "Estimation of land surface temperature from a Geostationary Operational Environmental Satellite (GOES-8)", *J. Geophys. Res*., vol. 108, 4326, doi: 10.1029/2002JD002422, 2003.

Sun, D. and R. T. Pinker, "Retrieval of surface temperature from the MSG-SEVIRI observations: Part I. Methodology". *Int. J. Remote Sens*., vol 28, 5255-5272, 2007.

Stoll, M.P., "Potential of remote sensing in the thermal band for global change". In: Vaughan, R.A., & Cracknell, A.P. (Ed.), Remote sensing and global climate change, NATO Advanced Science Institutes Series, Series I, vol. 24, pp. 393-404, Berlin, Springer Verlag, 1994.

Trigo, I. F. and P. Viterbo, "Clear-Sky Window Channel Radiances: A Comparison between Observations and the ECMWF Model", *J. Appl. Meteor*., vol. 42, 1463–1479, 2003

Trigo, I. F., L. F. Peres, C. C. DaCamara, and S. C. Freitas, "Thermal Land Surface Emissivity Retrieved From SEVIRI/Meteosat.", *IEEE Trans. Geosci. Remote Sens*., vol 46, doi: 10.1109/TGRS.2007.905197, 2008a.

Trigo, I. F., I. T. Monteiro, F. Olesen, and E. Kabsch, "An assessment of remotely sensed Land Surface Temperature", *J. Geophys. Res*., vol 113, D17108, doi:10.1029/2008JD010035, 2008b.

Wan, Z. and J. Dozier, 1996, "A generalized split-window algorithm for retrieving land surface temperature from space", *IEEE Trans. Geosci. Remote Sens*., vol. 34, 892–905, 1996.

Wan, Z., P. Wang, and X. Li, "Using MODIS land surface temperature And Normalized DifferenceVegetation Index products for monitoring drought in the southern Great Plains, USA", *Int J. Remote Sens*., vol. 25, 61-72, 2004.

Yu, Y., J. L. Privette, and A. C. Pinheiro, "Evaluation of Split-Window Land Surface Temperature Algorithms for Generating Climate Data Records", *IEEE Trans. Geosci. Remote Sens*., vol. 46, doi: 10.1109/TGRS.2007.909097, 2008.

Annex – SEVIRI/Meteosat LST Product: LSA-001 (MLST)

MLST uses emissivity, EM, as input. EM ALG is based on VCM that is a computationally efficient algorithm since estimation of IR radiances does not require any radiative transfer simulations and atmospheric corrections. EM is estimated daily, using daily values of FVC. The LST ALG then uses the most recent EM available. The main steps of EM ALG execution may be described as follows:

1 outer loop for MSG line
2 Inner loop for MSG column
- 2.1.selects FVC input file (static or dynamical file)
- 2.2 search for land pixels, skip and flag sea pixels
- 2.3 search for FVC pixel value, skip and flag missing values
- 2.4 search for Land Cover pixel value, skip and flag missing values
- 2.5.search for snow pixels from FVC error flag and land cover file
- 2.6 compute EM for IR10.8 and IR12.0, IR 3.9, IR 8.7 SEVIRI channels and IR broad band (3 -14 μm) using FVC
- 2.7. compute EM error bars
- 2.8 compute EM confidence level and perform QC

LST ALG is based on GSW that is computationally very efficient due to its linear form. The major steps of LST ALG execution may be described as follows:

1 outer loop for MSG line
2 Inner loop for MSG column
- 2.1 search for land pixels, skip and flag sea pixels
- 2.2 search for valid Tb, skip and flag corrupted Tb pixels
- 2.3 search for clear sky pixels, skip and flag cloudy pixels
- 2.4 search for emissivity pixel value, skip and flag missing values
- 2.5 compute LST with GSW
- 2.6. compute LST error bars
- 2.7 compute LST confidence level and perform QC

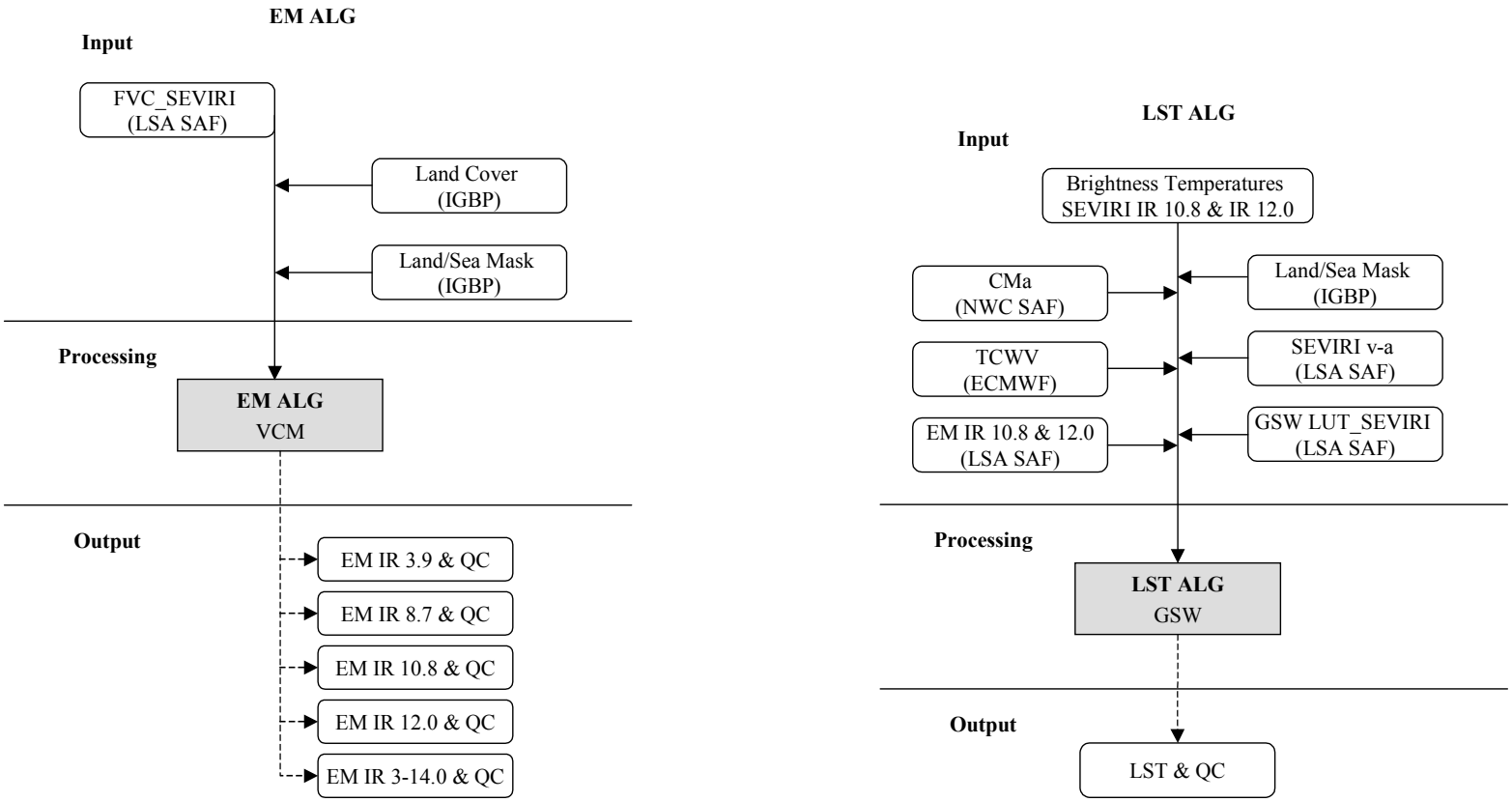

Figure 10. Diagram of processing chain, for SEVIRI/MSG retrieved EM (left) and LST (right).